Nanoscale

ROYAL SOCIETY OF CHEMISTRY

PAPER

View Article Online
View Journal | View Issue

Check for updates

Cite this: *Nanoscale*, 2025, **17**, 12323

Topical application of insulin encapsulated by chitosan-modified PLGA nanoparticles to alleviate alkali burn-induced corneal neovascularization†

Yuqing Zhang, ‡[a,b,c] Yangrui Du,‡[a] Sijie Zhou,[a] Zeqi Liu,[a] Pan Li[b] and Zhiyu Du*[a]

Received 31st December 2024,
Accepted 26th March 2025

DOI: 10.1039/d4nr05507a

rsc.li/nanoscale

Corneal neovascularization (CRNV) severely impairs corneal transparency and is one of the leading causes of vision loss worldwide. Drug therapy is the main approach to inhibit CRNV. Insulin (INS) has been reported to facilitate the healing of corneal injuries and suppress inflammation. However, but due to the unique physiological barriers of the eye, its bioavailability is low, limiting its therapeutic effect. In this study, we developed a chitosan-poly(lactic-*co*-glycolic acid)-INS nanoparticles (CPI NPs) system for INS delivery. The characterization of CPI NPs was satisfactory. Experimental results demonstrated that CPI NPs effectively inhibited the migration of vascular endothelial cells and the formation of tubular structures. Furthermore, CPI NPs markedly suppressed the neovascularization in a CRNV model without any observable side effects. Quantitative proteomics analysis indicated that INS treatment led to a reduction in FTO levels within the neovascularized cornea. Both *in vitro* and *in vivo* experiments substantiated the impact of CPI NPs on FTO protein expression and the N6-methyladenosine modification. In conclusion, this study successfully developed an effective ocular drug delivery system for the treatment of CRNV induced by alkali burns, thereby offering a novel therapeutic option for this condition.

1. Introduction

Corneal neovascularization (CRNV) is a pathological angiogenesis that severely impinges on corneal transparency and represents one of the primary contributors to vision loss globally.[1] In healthy corneas, an equilibrium between pro-angiogenic and anti-angiogenic factors is essential for sustaining the avascular condition of the corneal tissue.[2] In pathological conditions such as chemical injury, oxidative stress, infection, and immune disorders, the balance is disrupted, causing blood vessels from the limbal capillaries to invade the cornea's clear area, resulting in CRNV.[3] Chemical injury, particularly corneal alkali burn, is one of the main causes of CRNV and severely affects ocular structure and visual function. Conservative treatments often prove ineffective, resulting in vision impairment or blindness.[4] Following alkali burns, there is an activation of inflammatory cells, mesenchymal cells, activated keratinocytes, macrophages, and neovascular factors.[5] In addition, injuries to the conjunctival and corneal epithelium resulting from alkali burns can lead to a deficiency of limbal stem cells, which may subsequently contribute to corneal opacification and neovascularization.[6] Current clinical interventions for CRNV encompass a range of strategies, including topical corticosteroids, anti-vascular endothelial growth factor (VEGF) drugs, photodynamic therapy, laser photocoagulation, corneal transplantation, and amniotic membrane transplantation.[7] However, these treatments have limited clinical efficacy and several drawbacks. Long-term use of corticosteroids may lead to corneal perforation, increased intraocular pressure, and even glaucoma.[5] The clinical efficacy of anti-VEGF drugs is limited because they regulate only one pathway that controls angiogenesis, their inability to attenuate the inflammatory response, and the necessity for repeated administrations to sustain therapeutic benefits.[8,9] Consequently, there is a pressing necessity to identify more effective and safer treatment methods.

Insulin (INS) is a biologically active polypeptide that plays a vital role in the regulation and maintenance of cell growth, proliferation, and metabolism.[10] In the eye, INS is present in the tear film, and its receptors are localized in the ocular

---

[a] *Department of Ophthalmology, the Second Affiliated Hospital of Chongqing Medical University, Chongqing 400010, China. E-mail: 300074@hospital.cqmu.edu.cn*
[b] *Chongqing Key Laboratory of Ultrasound Molecular Imaging, Institute of Ultrasound Imaging, the Second Affiliated Hospital of Chongqing Medical University, Chongqing 400010, China*
[c] *State Key Laboratory of Ultrasound in Medicine and Engineering, Chongqing Medical University, Chongqing 400010, China*

† Electronic supplementary information (ESI) available. See DOI: **https://doi.org/10.1039/d4nr05507a**

‡ These authors contribted equally to this work.

surface tissues, with particularly high concentrations observed in the corneal epithelium.[11,12] Although INS is primarily recognized as a therapeutic agent for the management of diabetes, it has also been implicated in a diverse array of other research domains. In a seminal study conducted in 1945, researchers explored the potential of this hormone to promote the healing of corneal ulcers, thereby establishing a foundation for subsequent research into its applications within the field of ophthalmology.[13] Over the past two decades, there has been a significant increase in the topical application of INS for the treatment of corneal ulcers.[14] Yang *et al.* found that INS enhanced corneal epithelial healing and nerve repair in diabetic mice.[10] Balal *et al.* reported that INS eye drops are safe and effective treatment for persistent corneal epithelial defects caused by chemical injury.[15] Furthermore, a recent clinical study has demonstrated that topical INS can safely facilitate the healing of persistent epithelial defects that are unresponsive to conventional treatments, exhibiting superior efficacy compared to autologous serum.[16] Song *et al.* discovered that INS protected diabetic rats from oxidative stress and significantly reduced H_2O_2-induced cell apoptosis and reactive oxygen species, potentially treating diabetes-related cognitive decline.[17] Nevertheless, there is a paucity of literature regarding the application of INS in the treatment of alkali burn-induced CRNV. Additionally, it is worth noting that only 5% of the administered drop dosage affects the corneal surface. A large portion of the medication drains through the tear ducts, leading to low corneal absorption. Subsequent studies have demonstrated that topical INS drops do not influence blood glucose levels and show a high degree of safety.[14,18] Consequently, we propose the hypothesis that enhanced INS bioavailability may enable topical INS to effectively and safely treat alkali burn-induced CRNV.

Topical administration is widely regarded as the preferred approach for treating corneal diseases due to its ease of application and noninvasive characteristics.[19] Nevertheless, ocular drugs have low bioavailability when administered as eye drops. This limited absorption is attributed to several ocular barriers, such as tear turnover, nasolacrimal drainage, and the protective layers of the conjunctiva and cornea.[20] Enhancing drug retention and penetration on the ocular surface is crucial for overcoming barriers to eye drop administration and improving bioavailability.[21] Nanodrugs, nanoparticles (NPs) with encapsulated drugs, can solve this issue. The polymeric material poly(lactic-*co*-glycolic acid) (PLGA), recognized for its biocompatibility and biodegradability, has been approved by the FDA for application in ocular drug delivery systems and represents the most extensively employed nanocarrier system.[22] PLGA is composed of monomers derived from lactic and glycolic acids, which can be readily metabolized by the body. The use of PLGA-based NPs for ophthalmic drug delivery offers numerous advantages, including protecting encapsulated pharmaceuticals from rapid inactivation, providing sustained drug release through polymer degradation, and facilitating targeted delivery to specific regions or cells through surface modifications. Additionally, PLGA NPs exhibit high encapsulation efficiency for both hydrophilic and hydrophobic drugs, including macromolecules, proteins, peptides, and nucleic acids.[23] Numerous studies have focused on PLGA-based drug delivery systems for treating various diseases. A curcumin delivery system using PLGA has shown promise for Alzheimer's treatment due to its safety, efficacy, and affordability.[24] PLGA nanospheres with paclitaxel offered a slow, continuous release, enhancing antitumor effects and minimizing side effects compared to traditional methods.[25] Additionally, mannose-modified PLGA NPs carrying hepatitis B antigens effectively targeted epidermal antigen-presenting cells, improved antigen uptake, and triggered a robust immune response.[26] The findings from these studies collectively suggest that PLGA nanoparticle systems possess considerable advantages and promise for diverse drug delivery applications. To date, extensive modifications of PLGA have been undertaken to improve its efficacy as a drug delivery system, encompassing strategies such as surface modification, coating, blending, functionalization, and crosslinking.[27] For instance, the application of polyethylene glycol as a coating significantly extended the circulation time of PLGA NPs *in vivo* while simultaneously mitigating immune responses. Additionally, the use of chitosan or alginates as coatings enhanced the mucosal adhesion properties of PLGA, thereby facilitating targeted delivery to mucosal surfaces.[28] The surfaces of both PLGA NPs and the cornea, as well as the conjunctiva, possess a negative charge. Consequently, nanoparticle preparations using PLGA carriers can be quickly washed away by tears.[29] Therefore, to achieve stronger bond formation and extended retention time, modifying the surface properties of PLGA NPs is important, and positively charged formulations must be used. Cationic polymer coating is an effective method to modify the surface charge of PLGA NPs. Chitosan (CS), a material derived from chitin, has natural positive charges on its surface.[30] In addition, CS exhibits excellent antibacterial, anti-inflammatory, and biological adhesion properties, along with effective hemostatic capabilities.[31]

In this study, we prepared CS-PLGA-INS NPs (CPI NPs) using the double-emulsion method. We believe that CPI NPs possess anti-inflammatory properties and can inhibit neovascularization. Since proteins serve as primary drug targets in various disease conditions,[32] we employed proteomics to investigate the potential mechanisms through which CPI NPs may treat alkali burn-induced CRNV.

2. Experimental section

2.1. Materials

Poly(lactic-*co*-glycolic acid) (PLGA) (50 : 50, MW: 15 000) was purchased from Jinan Daigang Biomaterial Co., Ltd (Shandong, CN). Chitosan (deacetylation degree ≥95%) was purchased from Macklin (Shanghai, CN). Dichloromethane (DCM), poly(vinyl alcohol) (PVA), and isopropyl alcohol were purchased from Chuandong Chemical (Chongqing, CN).

Human recombinant INS was obtained from Sigma-Aldrich (St Louis, MO, USA). 1,1′-Dioctadecyl-3,3,3′,3′-tetramethylindocarbocyanine perchlorate (DiI) and 2-(4-amidinophenyl)-6-indolecarbamidine dihydrochloride (DAPI) were purchased from Beyotime (Shanghai, CN). 1.1′-Dioctadecyl-3,3,3′,3′-tetramethylindotricarbocyanine iodide (DiR) was purchased from Meilun Biotechnology Co., Ltd (Dalian, CN). All other reagents were at least of analytical grade.

2.2. Preparation of CPI NPs

PLGA NPs were produced using a double-emulsion technique with a water/oil/water system. Initially, 50 mg of PLGA was completely dissolved in 2 mL of DCM, and DiI or DiR dyes were incorporated as needed. Next, 1 mL of INS solution (5 mg mL^{-1}) was added, and the mixture was sonicated with a probe at 40 W (5 s on, 5 s off) for 3 min to generate the primary emulsion. The primary emulsion was further mixed with 4 mL of PVA solution *via* ultrasonication to produce multiple emulsions. Finally, 8 mL of 2% isopropanol aqueous solution was added to the multiple emulsions. The mixture was stirred magnetically for 3 h to evaporate the DCM. The resulting NPs were collected by centrifugation (12 000 rpm, 4 °C, 20 min), freeze-dried and weighed to obtain PLGA-INS NPs (PI NPs). PLGA NPs were synthesized without INS.

Afterward, the PI NPs were stirred and incubated (1 : 1, v/v) with 1 mg mL^{-1} CS solution (containing 1% glacial acetic acid) for 1 h. The CPI NPs were then washed twice with sterile water. Similarly, CS-PLGA NPs (CP NPs) were prepared as described above, but without INS. After lyophilization, the prepared NPs were sealed and stored at −20 °C for further use.

2.3. Characterization of CPI NPs

The size distribution, polydispersity index (PDI) and zeta potential of the PLGA NPs, PI NPs, and CPI NPs were analyzed using dynamic light scattering (DLS, Malvern, Zetasizer nano ZS90). The structure and morphology of the NPs were characterized by transmission electron microscopy (TEM) (FEI Tecnai G2 spirit, USA). The dried samples were subjected to Fourier transform infrared (FTIR) spectroscopy (Nicolet IS 10, USA), with spectral range of 500–4000 cm^{-1} and resolution better than 0.4 cm^{-1}.

The encapsulation efficiency (EE) and drug loading capacity (DLC) of INS in NPs were determined using an indirect method. The CPI NPs suspensions were centrifuged at 12 000 rpm for 20 min at 4 °C, and the clear supernatant was collected. The content of free INS in the clear supernatant was measured using high-performance liquid chromatography (HPLC) (Agilent 1260, USA), and the column was Hypersil ODS C18 (200 × 4.6 mm, 5 μm). The mobile phase consisted of a blend of water, acetonitrile, and trifluoroacetic acid at a ratio of 82 : 18 : 0.3. The flow rate was set at 1.0 mL min^{-1}, with detection performed at a wavelength of 210 nm. A 20 μL of the clear supernatant was injected into the HPLC system. The peak area corresponding to INS was measured, and the INS concentration was determined using a standard curve. The EE and DLC of the INS were calculated according to the following equations:

$$\text{EE}\,(\%) = (\text{total drug} - \text{free drug})/\text{total amount of drug} \times 100\%$$

$$\text{DLC}\,(\%) = (\text{total drug} - \text{free drug})/\text{NPs weight} \times 100\%$$

To determine the release of INS from the NPs, the CPI NPs were placed in dialysis membranes (MWCO 10 000), immersed in 50 mL of phosphate buffer saline (pH 7.4), and then incubated on a shaker at 37 °C (100 rpm). At predetermined times, samples were collected. The INS concentration in the samples was analyzed using HPLC, and the total INS released from the NPs was calculated. The cumulative percentage of INS released over time was then plotted.

2.4. Cell culture and cytotoxicity detection

Human umbilical vein endothelial cells (HUVECs) were cultured in DMEM (Gibco, USA), supplemented with 10% FBS (Gibco, USA) containing 1% penicillin and 1% streptomycin, and incubated at 37 °C in a humidified incubator with 5% CO_2. HUVECs were seeded at a density of 1×10^4 cells per well in 96-well culture plates and incubated overnight, followed by incubation with different formulations (INS, CP NPs, CPI NPs) at various concentrations. After 24 h of incubation, 100 μL of CCK-8 (APE × BIO, USA) solution (10% in medium) was added to each well, and the mixture was cultured for 3 h. Finally, cell viability was determined by measuring the absorbance at 450 nm using a microplate reader (HR801, CN). Triton X-100 (0.5%) served as the positive control. For lipopolysaccharide (LPS) treatment, the cells were stimulated with 500 ng mL^{-1} LPS for 6 h.

2.5. Cellular uptake of CPI NPs

The intracellular uptake of CPI NPs was observed using a laser confocal scanning microscope. HUVECs in the logarithmic growth phase were seeded at a density of 1×10^5 cells per confocal dishes and randomly assigned to the PI NPs group or the CPI NPs group (all the NPs were stained with DiI [$\lambda_{\text{excitation}}/\lambda_{\text{emission}}$ = 550 nm/567 nm]). After 3 h of culture, the medium was replaced with medium containing either PI NPs or CPI NPs. After a specified duration, the cells were rinsed with PBS and then fixed immediately with 4% paraformaldehyde for 10 min. Nuclei were stained with DAPI ($\lambda_{\text{excitation}}/\lambda_{\text{emission}}$ = 364 nm/454 nm), and the process of cellular uptake was examined using a confocal laser scanning microscope (CLSM) (Olympus).

2.6. Retention of CPI NPs on ocular anterior segments

Fluorescence imaging was conducted *in vitro* using the Berthold Night OWL LB 983 system (Germany) to capture ocular fluorescence at various time intervals. Sprague-Dawley (SD) rats were divided into two groups, with three rats in each group. After sedation with pentobarbital sodium, 5 μL of DiR-labeled PI NPs or CPI NPs was instilled into the right eye, and imaging was conducted at 0 h, 0.5 h, 1 h, 2 h, and 3 h.

2.7. Migration, and tube formation assays

Wound healing assay. HUVECs (5×10^5 cells per well) were seeded into a 6-well plate and cultured overnight until the confluence reached approximately 90%. The cell monolayer wound was created in each well, and the plates were gently washed three times with 1× PBS. Then, the cells were treated with LPS and different formulations (PBS, INS, CP NPs, CPI NPs). The cells were incubated at 37 °C, and imaging was performed using an inverted microscope at 0 and 24 h.

$$m\ (\%) = (1 - n/r) \times 100\%,$$

where n represented the width of the scratch at 24 h, m represented the migration of HUVECs, and r represented the initial scratch width.

Transwell assays. LPS-treated HUVECs were seeded into the upper chamber of a transwell (pore size 8 μm) at a density of 2×10^4 cells, and incubated at 37 °C for 24 h in the aforementioned different formulation media. The migrated cells were then fixed with 4% paraformaldehyde and subsequently stained with crystal violet. Following three washes with PBS, the stained samples were examined under a microscope.

Tube formation assay. Prior to the experiment, 24-well plates were precooled, and Matrigel was added to the bottom of each well, followed by incubation at 37 °C for 1 h to allow for solidification. LPS-treated HUVECs (8×10^4 cells per well) were mixed with the different formulations described above and seeded into the wells of the 24-well plate, followed by incubation for 4 h. Tube formation was observed using an inverted microscope, and the number of junctions and nodes was calculated using Image J.

2.8. ELISA

HUVECs (1×10^5 cells per well) were seeded into 48-well plates and cultured overnight. The cells were then stimulated with LPS for 6 h. After 6 h of LPS stimulation, the medium was discarded, and the HUVECs were cocultured with different media (PBS, INS, CP NPs, CPI NPs) for 24 h. The supernatant from each well was then collected, and the levels of TNF-α and IL-6 in the supernatant were detected using commercial ELISA kits according to the procedures provided by the manufacturers. Each experiment was conducted in triplicate.

On day 14, the corneas from each group were quickly frozen in liquid nitrogen and homogenized with 500 μL of PBS. A low-temperature centrifuge was used to centrifuge the mixture at 10 000*g* for 10 min at 4 °C, and the supernatant was collected. The levels of TNF-α and IL-6 in the supernatant were subsequently measured using commercial ELISA kits according to the manufacturer's instructions.

2.9. Induction of CRNV

Male SD rats (7–8 weeks old) were obtained and housed at the Animal Experiment Center of Chongqing Medical University (Chongqing, China). The experiments were performed following the guidelines provided in the Guide for the Care and Use of Laboratory Animals. All experiments were approved by the Ethics Committee (Approval No: IACUC-CQMU-2024-0037) of the Second Affiliated Hospital of Chongqing Medical University.

We employed the alkali burn method to induce a rat model of CRNV. The rats were anesthetized with intraperitoneal injection of pentobarbital (30–50 mg kg^{-1}). A 3 mm diameter filter paper saturated with 1 N NaOH was placed on the central cornea of the right eye for 30 s, followed by an immediate thorough rinse with a large quantity of sterile saline for 1 min, the left eye received no treatment. Levofloxacin eye drops were administered following surgery to prevent infection. The rats were randomly divided into five groups (PBS, dexamethasone sodium phosphate (Dexp), INS, CP NPs and CPI NPs). Each group received treatment three times daily for 14 consecutive days according to the specified formulation after the alkali burn.

2.10. Clinical evaluations of CRNV

The corneal opacity, corneal epithelial defect, and CRNV area in the treatment and control groups were continuously observed, assessed, and documented with photographs. The intraocular pressure (IOP) was measured using a handheld tonometer (iLab tonometer; iCare).

Corneal opacity was scored on a scale of 0–4.[33] 0 = completely clear; 1 = slightly hazy, iris and pupil easily visible; 2 = slightly opaque, iris and pupil still detectable; 3 = opaque, pupils hardly detectable; and 4 = completely opaque with no view of the pupil.

For corneal epithelial defect, alkali-burned corneas were examined before and after fluorescein staining using a portable slit lamp and documented with photographs. The intact corneal epithelium remained unstained, whereas the damaged areas appeared green in patchy or dot-like patterns.

The corneal epithelial defect rate was calculated according to the following formula:

$$S = S_{\mathrm{t}}/S_0 \times 100\%,$$

where S_{t} is the stained area observed and S_0 is the baseline-stained area.

For the CRNV area, the area of CRNV (S) was quantified *via* the formula $S = C/12 \times \pi \times [r^2\ (r - \mathrm{l})^2]$. In this context, S denotes the area of CRNV, C indicates the number of circumferential hours of neovascularization affecting the cornea, l refers to the length of neovascularization extending from the limbus into the cornea, and r represents the corneal radius.[34] Both the corneal radius and the length of neovascularization were assessed using Image J imaging software.

2.11. Histopathology and immunofluorescence assay

Hematoxylin–eosin (HE) staining was performed as previously described.[35] In brief, the rats were euthanized on days 7 and 14. The eyeballs were sectioned within 30 min, fixed overnight in 4% paraformaldehyde, and then embedded in paraffin at a thickness of 4 μm. The sections were treated with hematoxylin and eosin and observed under a light microscope.

An immunostaining assay was conducted to evaluate the expression of VEGF and CD31. As mentioned above, the rats were euthanized on days 7 and 14. The eyeball sections were fixed in 4% formaldehyde, embedded in optimal cutting temperature medium, and sliced into 5 μm thick sections. The samples were pretreated with 1% Triton, followed by incubation in a 5% goat serum solution. The expression of CD31 and VEGF was detected using CD31 and VEGF-A antibodies, respectively. After the immunostaining procedure, images were captured using confocal microscopy (AX, Nikon).

2.12. Western blotting

Proteins from cells and corneal tissue were extracted using RIPA buffer (Beyotime, CN) supplemented with protease inhibitors. The protein concentration was measured using a BCA assay kit (KGB2101, CN). Proteins (20 μg per lane) were separated on 4–12% SDS-PAGE gels and transferred to PVDF membranes (Millipore, USA). The PVDF membranes were blocked with QuickBlock™ Blocking Buffer (Beyotime, CN) for 30 min at room temperature. Then, the samples were incubated at 4 °C overnight with the corresponding primary antibodies. The membrane was washed with TBST and then incubated with HRP-conjugated secondary antibodies (Proteintech, 1 : 2000, Cat. No. SA00001-2) at room temperature for 2 h. Blotting images were captured using an enhanced chemiluminescence detection reagent (Beyotime, CN). Finally, the band intensities were measured using Image J.

2.13. RNA extraction, reverse transcription, and qRT-PCR

Total RNA was isolated from cells and corneal tissues using TRIzol reagent (Thermo Fisher Scientific, Waltham, MA, USA), following the manufacturer's guidelines. After RNA extraction, DNase I was utilized to eliminate any residual DNA. The quality of the RNA was evaluated by measuring the A260/A280 ratio with a NanoDrop® ND-1000. The total RNA was subsequently reverse-transcribed into cDNA using the PrimeScript™ RT Master Mix (RR036A, Takara Biotechnology Co., Ltd, Dalian, CN) according to the manufacturer's instructions. qRT-PCR was conducted with TB Green® Premix Ex Taq™ II (RR820A, Takara Biotechnology Co., Ltd, Dalian, CN) and LightCycler 480 system (LightCycler 480 software 1.5, Roche, Basel, Switzerland). The conditions of the qRT-PCR cycle included a predenaturation step at 95 °C for 30 s followed by 40 cycles of 95 °C for 5 s and 60 °C for 20 s.

2.14. *N*6-Methyladenosine (m6A) quantification

The global changes in m6A levels across total mRNA were measured using the EpiQuik m6A RNA Methylation Quantification Kit (Colorimetric) (Epigentek, Farmingdale, NY, USA) according to the manufacturer's instructions. A 200 ng sample of RNA was analyzed, and m6A signals were detected at 450 nm.

2.15. LC-MS/MS analysis

The tryptic peptides were dissolved in solvent A and subsequently loaded onto a home-made reversed-phase analytical column (25cm in length, 100 μm i.d.). The mobile phase was composed of solvent A (0.1% formic acid, 2% acetonitrile in water) and solvent B (0.1% formic acid, 90% acetonitrile in water). Peptides were separated with the following gradient: 0–22.5 min, 6%–22% B, 22.5–26.5 min, 22%–34% B, 26.5–28.5 min, 34%–80% B, 28.5–30 min, 80% B, with a constant flow rate of 700 nl min^{-1} on an EASY-nLC 1200 UPLC system (Thermo Fisher Scientific). The separated peptides were analyzed using an Orbitrap Exploris 480 mass spectrometer equipped with a nanoelectrospray ionization source. The electrospray voltage applied was 2300, and the FAIMS compensation voltage was set as −45 V. Both precursors and fragments were analyzed using the Orbitrap detector. The full MS scan resolution was set to 60 000 for a scan range of 350–1400 *m*/*z*. The MS/MS scan was fixed first mass as 120.0 *m*/*z* at a resolution of 15 000. HCD fragmentation was performed at a normalized collision energy (NCE) of 27%. The automatic gain control target was set at 1E6, with a maximum injection time of 22 ms. All the LC-MS/MS data were analysed using the DIA-NN search engine (v.1.8).

2.16. Biocompatibility

To conduct a comprehensive assessment of drug safety, the rats were randomly divided into six groups: normal, PBS, Dexp, INS, CP NPs and CPI NPs. One drop of the formulation (approximately 10 μL) was applied to each eye three times daily for a continuous duration of 14 days. On day 14, the corneas of the rats in each group were examined using a slit lamp microscope, and fluorescein sodium staining was performed to assess the integrity of the corneal epithelium. The rats were subsequently sacrificed, and their right eyes were dissected for corneal HE staining.

Blood samples were collected to evaluate the levels of white blood cells, red blood cells, platelets, aspartate aminotransferase, blood urea nitrogen, and creatinine. Furthermore, five visceral organs, including the heart, liver, spleen, lungs, and kidneys, were excised for HE staining.

2.17. Degradation behavior for CPI NPs

The degradation behavior of NPs was evaluated by the reduction of nanoparticle mass over time following *in vitro* culture in PBS (pH 7.4). The CPI NPs sample (3ml), encapsulated in a dialysis membranes (MWCO 10 000), was incubated in 30ml PBS at 37 °C with gentle agitation in a water bath. The nanoparticle samples were removed from the incubation medium at predetermined intervals (1, 7, 14 and 21 days) and freeze-dried. The residual weight percentage of the sample within 0–21 days of degradation is calculated as follows: residual weight (%) = $(W_t \times 100)/W_0$, where W_t is the dry weight of the sample after degradation, and W_0 is the initial weight.

For *in vivo* circulation, DiI-CPI NPs were administered *via* rat tail vein at a total dose of 500 μg. At various time intervals (24, 48, 72, and 96 h), the tails of the rats were punctured, and 20 μL of whole blood was collected and placed in anticoagulation tubes. The fluorescence intensity of the remaining NPs in the blood was subsequently measured using a fluorescence microplate reader.

2.18. Statistical analysis

All experiments were bioreplicated at least 3 times. The data were expressed as mean ± standard deviation. Statistical analysis was performed using GraphPad 9.5 software (GraphPad software, San Diego, USA). One-way analysis of variance and Tukey's multiple comparison test were used for multigroup comparison. $p < 0.05$ was considered statistically significant.

3. Results and discussion

3.1. Characterization of CPI NPs

Initially, INS was encapsulated within PLGA using a double emulsion technique to fabricate PI NPs. Subsequently, CS was adsorbed onto the surface of the PI NPs *via* electrostatic interactions, resulting in the formation of CPI NPs (Fig. 1A). The zeta potentials of the PLGA NPs, PI NPs, and CPI NPs were measured to be −14.00 ± 0.62 mV, −2.01 ± 0.05 mV, and +11.80 ± 2.08 mV, respectively (Fig. 1B and Table 1). TEM images demonstrated that the PLGA NPs, PI NPs, and CPI NPs possessed a smooth, round morphology and exhibited excellent dispersion. Furthermore, the surface of the CPI NPs was characterized by a uniform CS coating, as illustrated in Fig. 1C. The particle size of the PLGA NPs, PI NPs, and CPI NPs were measured as 141.4 ± 8.4 nm, 181.0 ± 5.5 nm, and 213.9 ± 7.5 nm, respectively (Fig. 1E). All NPs exhibited polydispersity index (PDI) values below 0.2, indicating a uniform particle size distribution. The INS EE of the CPI NPs was 50.28 ± 2.49%, and the INS DLC of the CPI NPs was 4.42 ± 0.22%. PLGA exhibit a negative charge attributable to their terminal carboxyl groups, facilitating the adsorption of positively charged CS for surface modification. The electrostatic interaction between CS and PLGA leads to charge neutralization, subsequently reversing the zeta potential to a positive value and increasing the particle size.[36] Particle size and zeta potential are critical parameters in the assessment of NPs. Particles exceeding 1 μm in diameter are unable to penetrate the corneal barrier.[37] NPs of excessive size may obstruct light

Table 1 Mean size, PDI, zeta potential, EE and DLC of NPs ($n = 3$)

Nanoparticles	Size (nm)	PDI	Zeta potential (mV)	DLC (%)	EE (%)
PLGA NPs	141.4 ± 8.4	0.117 ± 0.014	−14.00 ± 0.62	—	—
PI NPs	181.0 ± 5.5	0.045 ± 0.043	−2.01 ± 0.05	—	—
CPI NPs	213.9 ± 7.5	0.120 ± 0.023	+11.80 ± 2.08	4.42	50.28

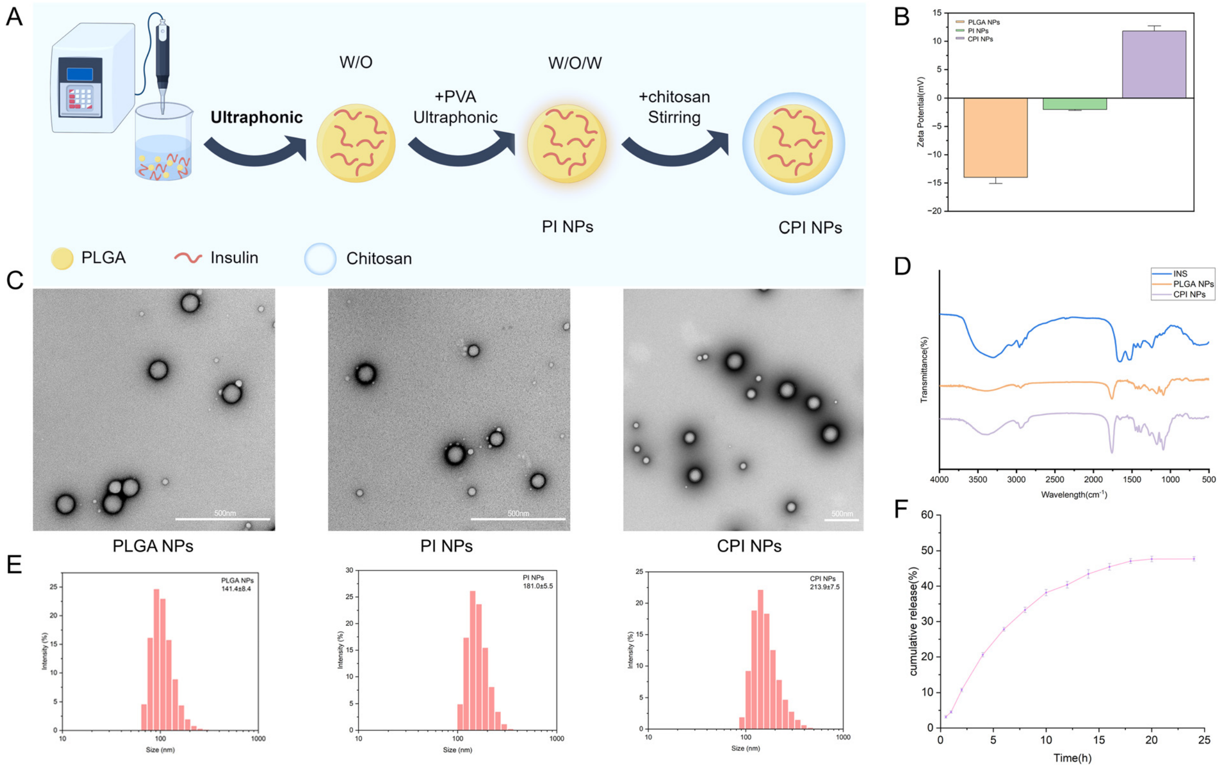

Fig. 1 Preparation and characterization of CPI NPs. (A) Schematic representation of the design strategy for CPI NPs (Created by Figdraw). (B) Zeta potential measurements of PLGA NPs, PI NPs, and CPI NPs ($n = 3$ per group). (C) TEM images depicting the morphology of PLGA NPs, PI NPs, and CPI NPs. (D) FTIR spectra of INS, PLGA NPs, and CPI NPs. Scale bar: 500 nm. (E) Particle size analysis of PLGA NPs, PI NPs, and CPI NPs ($n = 3$ per group). (F) *In vitro* release profile of INS from CPI NPs ($n = 3$ per group).

transmission to the eye, cause significant irritation, compromise comfort, and diminish patient compliance and tolerance. The corneal surface generally possesses a negative charge, while the CPI NPs synthesized in our study exhibit a positive charge. This positive charge facilitates interaction with the negatively charged corneal surface, potentially enhancing the rapid distribution and prolonged retention of the drug on the ocular surface.

FTIR was employed to analyze the molecular structures of INS, PLGA NPs, and CPI NPs, as depicted in Fig. 1D. In this figure, the blue curve corresponds to the infrared spectrum of INS, while the orange curve represents the infrared spectrum of the PLGA NPs. There were absorption peaks of the amide I band (caused by C═O stretching vibration) and amide II band (caused by N–H bending vibration and C–N stretching vibration) at 1656 cm^{-1} and 1519 cm^{-1}, respectively. The two absorption peaks of the PLGA NPs at 1760 cm^{-1} and 1176 cm^{-1} were attributed to the C═O stretching vibration and C–O–C stretching vibration, respectively, which was consistent with the results of a previous study.[38] The purple curve represented the infrared spectrum of CPI NPs. The characteristic band of CS at 3350 cm^{-1} was attributed to the stretching vibrations of the O–H groups in CS.[39] The characteristic peaks of the PLGA and INS were present, with a slight shift observed in the characteristic peak of INS. No novel peaks were observed in the CPI NPs, suggesting that INS was effectively encapsulated within the PLGA NPs, which were in turn successfully coated by CS. The Fig. 1F showed the release profile of INS from CPI NPs in phosphate buffer saline (pH 7.4). The *in vitro* release behavior of the CPI NPs showed no significant burst release effect, with a cumulative release of 3.14% at 0.5 h, 10.71% at 2 h, and 47.71% at 24 h.

3.2. Cellular uptake and ocular anterior segment retention of CPI NPs

In this study, CLSM was employed to investigate the cellular uptake of NPs. Following a 3 h incubation with HUVECs, the DiI-PI NPs exhibited relatively weak orange-red fluorescence, whereas the DiI-CPI NPs demonstrated significantly enhanced fluorescence (Fig. 2A). The findings indicated that CPI NPs exhibited a higher uptake efficiency in HUVECs compared to PI NPs. The cell membrane is composed of a phospholipid bilayer with a negatively charged surface. As a result, the surface charge of NPs can significantly influence their interaction with the cell membrane, with positively charged CPI NPs demonstrating enhanced cellular uptake. For optimal treatment outcomes, it is crucial for NPs to be efficiently taken up and stored in target cells.[40]

Extending the retention time may enhance the ocular bioavailability of the drug.[41] Improving the retention of ocular pharmaceuticals in the cornea and conjunctiva to enhance their bioavailability and therapeutic efficacy in ocular tissues has become a key focus in drug delivery systems. In our study, we used a live fluorescence imaging system to assess the reten-

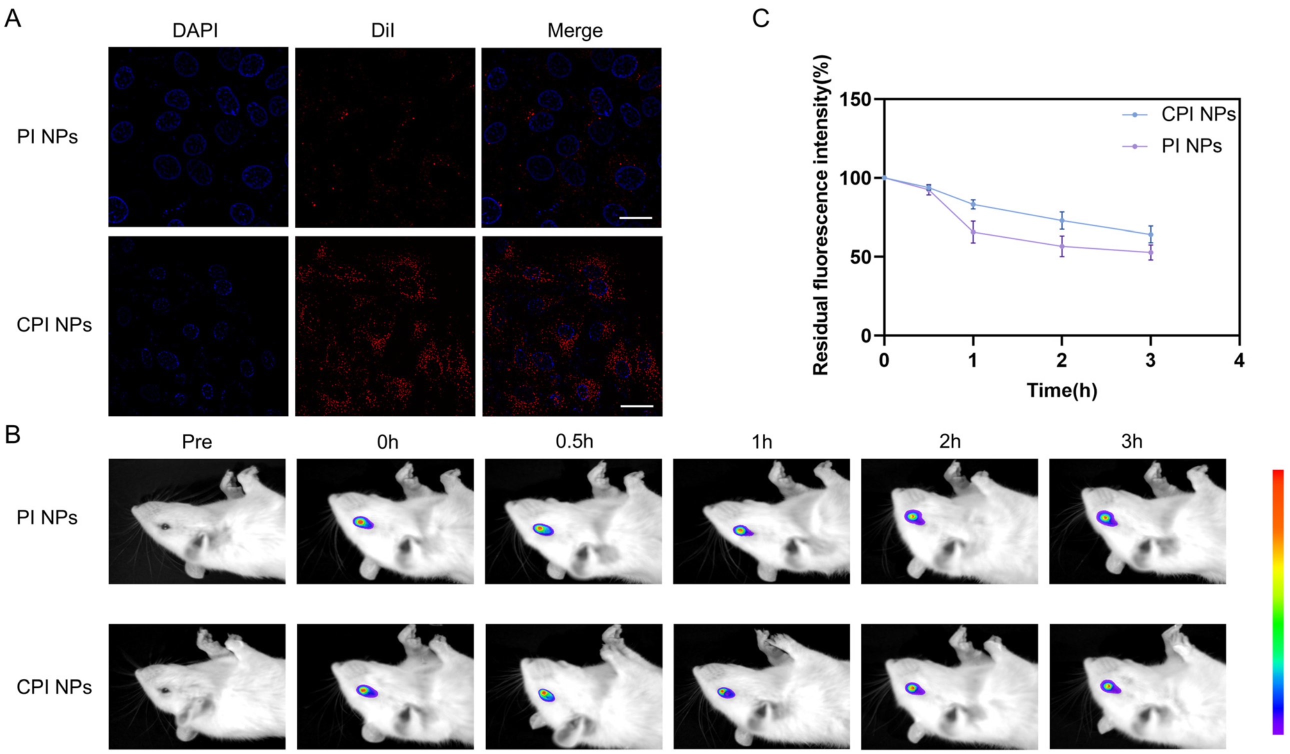

Fig. 2 Cellular uptake and retention of the CPI NPs. (A) CLSM images of intracellular in different groups at 3 h. Scale bar: 20μm. Representative fluorescenceimages of rat eyes (B) and quantification (n = 3 per group) of the residual fluorescence signal (C) at different time points after topical administration of the PI NPs or CPI NPs. Results were presented as the mean ± SD.

tion of the NPs. The fluorescence images captured at various time intervals, as illustrated in Fig. 2B, revealed a significant decrease in fluorescence intensity across all groups over time, with the fluorescence intensity of PI NPs diminishing at a faster rate than that of CPI NPs. The correlation between the percentage of residual fluorescence intensity and test duration, presented in Fig. 2C, further corroborated the findings depicted in Fig. 2B. After a duration of 2 h, the fluorescence intensity of DiR-PI NPs decreased by approximately 43% and continued to decline thereafter. At 3 h, the residual fluorescence intensity of DiR-PI NPs was approximately 52.81%, while that the fluorescence intensity of DiR-CPI NPs was approximately 64.20%. These results indicated that DiR-CPI NPs adhere to the corneal surface longer than DiR-PI NPs. This extended retention may facilitate deeper penetration of the INS into the corneal tissue, thereby enhancing therapeutic efficacy. Cationic NPs can increase the retention duration of drugs on the negatively charged corneal surface. Additionally, CS exhibits significant bioadhesive properties, further enhancing the contact time with the cornea.[42,43]

3.3. Evaluation of the efficacy of CPI NPs *in vitro*

To assess the *in vitro* cytotoxicity of the CPI NPs, we used a CCK-8 assay to assess the cell viability of the HUVECs. The cell viability of HUVECs treated with INS, CP NPs, and CPI NPs for a duration of 24 h were presented in Fig. 3A. In HUVECs, INS concentrations below 250 μg mL^{-1} did not significantly affect cell viability. However, at concentrations of 500 and 1000 μg mL^{-1}, a reduction in cell viability was observed. Following 24 h of incubation with CP NPs at varying concentrations, the group treated with 250 μg mL^{-1} of CP NPs exhibited the highest cell viability. Among the different concentrations of CPI NPs, those at or below 500 μg mL^{-1} did not significantly affect cell viability, whereas treatment with 1000 μg mL^{-1} of CPI NPs reduced cell viability to 84.25%. These findings provide preliminary insights into the safety parameters for subsequent experimental investigations.

In this study, we developed an *in vitro* inflammation model and conducted a preliminary assessment of the anti-inflammatory effects of CPI NPs. LPS was used to stimulate cytokine production in HUVECs, TNF-α and IL-6 levels were measured using ELISA after treatment with various formulations. Following LPS stimulation, there was a marked elevation in the concentrations of TNF-α and IL-6, with the highest TNF-α concentration observed in the LPS + PBS group and the highest IL-6 concentration in the LPS + CP NPs group. Administration of INS and CPI NPs resulted in a reduction of TNF-α and IL-6 levels. There was no statistically significant difference between

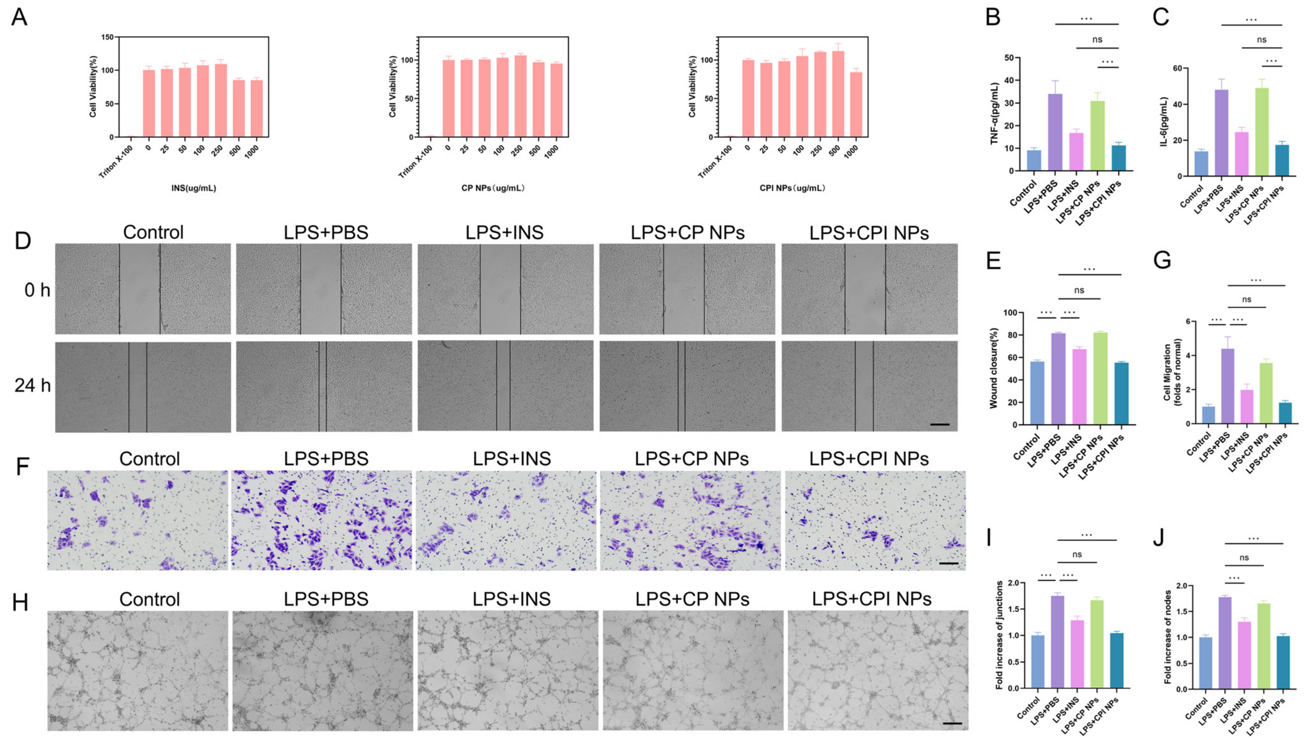

Fig. 3 Evaluation of the efficacy of the CPI NPs *in vitro*. (A) Cell viability of HUVECs after incubation with different concentrations of INS, CP NPs or CPI NPs 24h later ($n = 3$). Triton X-100 was used as the positive control samples. (B) TNF- α and IL-6 (C) in each group after treatment ($n = 3$ per group). (D) Images from wound healing assay were taken at 0 and 24h after scratching (scale bar: 200 μm). (E) Quantitative analysis of wound healing assays after different treatments ($n = 3$ per group). (F) Images of HUVECs in transwell migration assays after 24h (scale bar: 200 μm). (G) Quantitative analysis of the HUVECs migration ability ($n = 3$ per group). (H) Images of tube formation assay in HUVECs after different treatments (scale bar: 200 μm). Quantitative analysis of the numbers of junctions (I) and nodes (J) ($n = 3$ per group). The control group received no LPS treatment and was treated with PBS. Results were presented as the mean ± SD. ns indicates no significant difference. $^{*}p < 0.05$; $^{**}p < 0.01$; $^{***}p < 0.001$.

LPS + INS group and LPS + CPI NPs group. These findings indicate that INS and CPI NPs can attenuate the inflammatory response induced by LPS, with CPI NPs being the most effective (Fig. 3B and C).

Endothelial cells undergo proliferation, migration, and aggregation to establish initial vascular networks. Subsequently, these structures mature and undergo remodeling, a process characterized by the recruitment of smooth muscle cells, ultimately resulting in the formation of fully developed blood vessels.[44,45] HUVECs are widely used as endothelial cell models due to their strong representativeness. They effectively simulate the behavior and responses of vascular endothelial cells *in vivo*, particularly in the context of angiogenesis research. In this study, we conducted wound healing, transwell and tube formation assays *in vitro* to evaluate the impact of CPI NPs on the migration and tube formation of HUVECs. At 24 h, the scratch area in the LPS + PBS group was significantly reduced compared to the control group, and the reduction in scratch area in the LPS + CPI NPs group was significantly smaller than that in the LPS + PBS, LPS + INS and LPS + CP NPs groups (Fig. 3D). And the wound closure rate in the LPS + CPI NPs group was significantly lower than that in the LPS + PBS, LPS + INS, and LPS + CP NPs groups (Fig. 3E). The cell migration in the LPS + PBS group was significantly higher than that in the control group. And compared to the LPS + PBS group, the LPS + CPI NPs group exhibited a significantly reduced number of migrating cells (Fig. 3F and G). These results indicated that CPI NPs showed the best significant repression effect on endothelial cell migration.

To evaluate endothelial cell angiogenesis, the tube formation assay is commonly used as it mimics numerous steps in the angiogenesis process.[46] In this study, the ability of CPI NPs to inhibit angiogenesis was evaluated using a tube formation assay. Representative images of the tube formation assay were presented in Fig. 3H, while the quantification of junctions and nodes was illustrated in Fig. 3I and J. The results showed that LPS significantly enhanced the tubular formation ability of HUVEC cells compared to the control group. Many tube-like structural networks were observed in the LPS + PBS and LPS + CP NPs groups, but no significant difference was found in the number of junctions and nodes between the two groups. Compared with the LPS + PBS group, the number of junctions and nodes in the LPS + INS and LPS + CPI NPs groups was significantly reduced, with the fewest in the LPS + CPI NPs group. These results were generally consistent with the findings from the wound healing and transwell assays. The results of tube formation assay showed that CPI NPs had the strongest capability to inhibit tube formation of HUVECs.

3.4. *In vivo* efficacy evaluation of CPI NPs

To investigate the impact of CPI NPs on CRNV *in vivo*, male SD rats were randomly assigned to one of the following groups: PBS group (thrice daily), Dexp group (250 μg mL^{-1}, thrice daily), INS group (250 μg mL^{-1}, thrice daily), CP NPs group (250 μg mL^{-1}, thrice daily), and CPI NPs group (500 μg mL^{-1}, thrice daily). The determination of dosage was informed by preliminary experimental data and pertinent literature (ESI Fig. 1†).[47,48] A corneal alkaline burn model was employed to induce CRNV, with postoperative observations conducted over a 14-day period. After the alkali burn, the limbal vascular network rapidly grows on the cornea. On day 3, the corneal tissues in all the groups became cloudy and edematous, with a filled limbal vascular network. On day 7, there was a gradual reduction in inflammation. Improvements were observed in corneal opacity and edema, with the exception of the PBS group and the CP NPs group. Additionally, neovascularization became more pronounced compared to earlier observations. Hyphema was observed in both the PBS group and the CP NPs group. On day 14, there was no significant improvement in corneal opacity in both the PBS and CP NPs groups, with a substantial invasion of neovascularization invading the central corneal region. In contrast, the Dexp and INS groups exhibited a reduction in corneal edema, with neovascularization primarily affecting the peripheral cornea. Notably, in the CPI NPs group, edema had nearly completely subsided, and neovascularization was predominantly confined to the corneal limbus (Fig. 4A and B).

On day 7, the corneal opacity score was highest in the PBS group (3.67 ± 0.58) and lowest in the CPI NPs group (2.00 ± 0.00). On day 14, the corneal opacity score remained highest in the PBS group (4.00 ± 0.00), followed sequentially by the CP NPs group (3.67 ± 0.58) and the INS group (1.33 ± 0.58), with the CPI NPs group exhibiting the lowest score (0.33 ± 0.58) (Fig. 4C). There was no significant difference in baseline IOP among the different groups of rats. On day 14, the IOP measurements for the PBS, Dexp, and CP NPs groups were 38.40 ± 3.18 mmHg, 42.13 ± 3.33 mmHg, and 39.30 ± 2.69 mmHg, respectively, all of which exceeded the normal IOP range. Conversely, the IOP values for the INS and CPI NPs groups remained within the normal range (Fig. 4D).

Further quantification of the neovascularization area revealed that, at 14 days, the neovascularization area relative to the corneal area in the CPI NPs group was the smallest (20.91 ± 2.53)%, which was significantly lower than that observed in the PBS group (89.10 ± 2.95)%. Additionally, the neovascularization area in the CPI NPs group was lower than that in both the INS group (32.76 ± 2.00)% and the CP NPs group (87.30 ± 1.96)%, with these differences reaching statistical significance. However, no statistically significant difference was found between the CPI NPs group and the Dexp group (Fig. 4E).

The lack of significant improvement in corneal opacity observed in both the PBS group and the CP NPs group may be attributed to the extensive invasion of neovascularization into the central cornea, resulting in increased vascular permeability and heightened exudate accumulation. This process likely exacerbated corneal opacity and disrupted the normal arrangement of collagen fibers. Alkali burn injury of the cornea can induce significant infiltration of inflammatory cells, including neutrophils and macrophages, resulting in pronounced exudation within the anterior chamber.[49] This process may lead to narrowing of the anterior chamber angle , thereby elevating IOP. In severe instances, synechiae may form between the iris

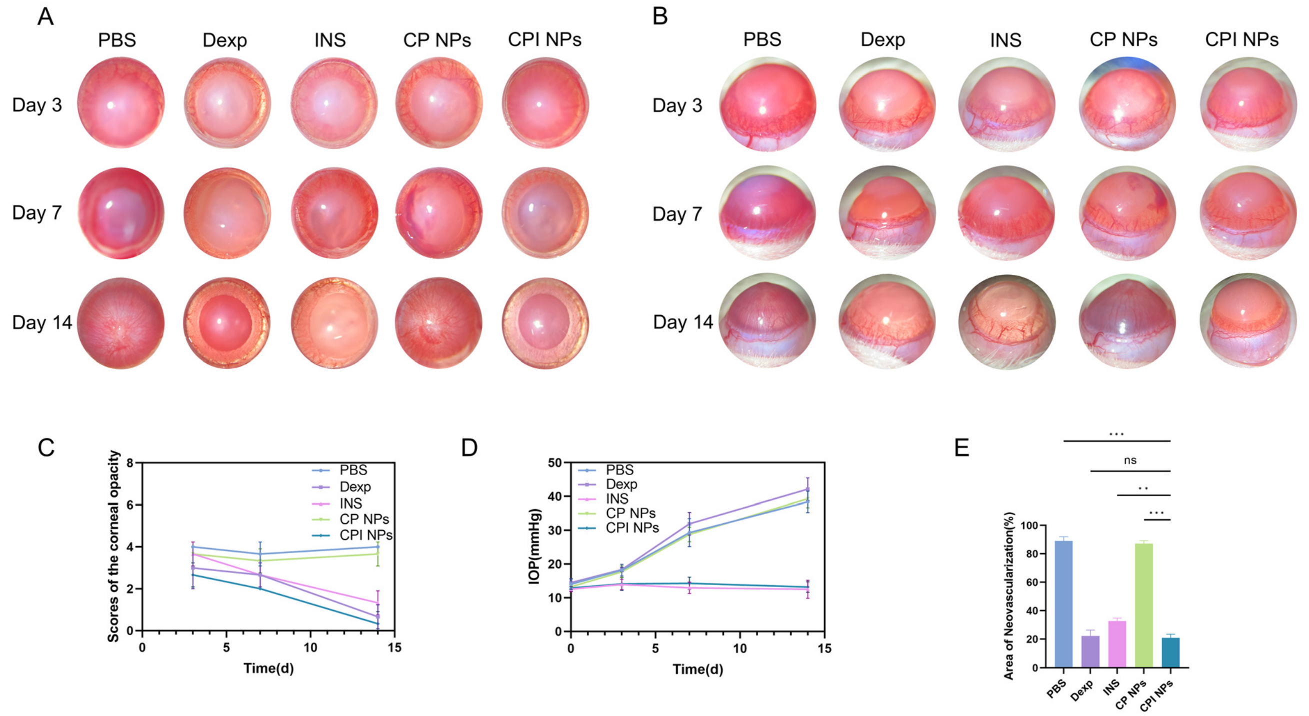

Fig. 4 The suppressive effect of the CPI NPs on CRNV. Slit lamp images of eyeballs viewed from above (A) and from the side (B). (C) Scores of the corneal opacity in each group at different time points (days 3, 7, and 14) (n = 3 per group). (D) IOP in each group at different time points (days 0, 3, 7 and 14) (n = 3 per group). (E) CRNV area ratio (n = 3 per group). Results were presented as mean ± SD. ns indicates no significant difference. *p < 0.05; **p < 0.01; ***p < 0.001.

or lens and the cornea may occur, which can potentially lead to the development of secondary glaucoma.[50] On the other hand, early direct chemical damage can lead to tissue atrophy and destruction of the trabecular meshwork and outflow pathways, and may also result in increased intraocular pressure.[51] In the INS group and the CPI NPs group, IOP remained within the normal range, potentially attributable to the anti-inflammatory properties of INS. This effect may effectively mitigate tissue damage resulting from corneal alkali burns and subsequently prevent an increase in IOP.

Fluorescein sodium staining was employed to assess the extent of corneal epithelial damage across the different groups (Fig. 5A). A comparative analysis of the rate of epithelial defects between different treatment groups was shown in Fig. 5B. On day 7, corneal epithelial repair was poor in the Dexp group. In comparison to prior observations, epithelial healing in the PBS, Dexp, and CP NPs groups did not improve as significantly as in the INS and CPI NP groups. Conversely, the INS and CPI NPs groups demonstrated a reduction in the area of epithelial defects. Throughout the corneal epithelial repair process, neither the PBS group nor the CP NPs group exhibited complete corneal epithelial healing. In the CPI NPs group, there were no signs of nonhealing during the corneal epithelial injury repair process. In the early stage of corneal alkali burn, various factors, including interleukins (IL-1β, IL-6, and IL-10), TNF-α, matrix metalloproteinases, and platelet-derived growth factor, become activated. These factors attract inflammatory cells, exacerbate the inflammatory process, and contribute to the development of CRNV.[52] On day 14, the concentrations of TNF-α and IL-6 were higher in the PBS group and CP NPs group. The concentrations of TNF-α and IL-6 in the CPI NPs group were lower compared to those observed in the PBS group, Dexp group, INS group, and CP NPs group, and the differences were statistically significant. These results indicated that CPI NPs exhibit anti-inflammatory properties (Fig. 5C and D).

To further evaluate the inhibitory effect of CPI NPs on neovascularization, we performed histopathological examination and immunofluorescence staining. On day 7, the corneal tissue structure in both the PBS and CP NPs groups exhibited significant disturbances, characterized by thickening and loosening of the stromal layer, extensive infiltration of inflammatory cells, and the formation of neovascular lumens. These changes were attributed to the poor structure and function of the neovascularization, which was characterized by increased permeability and a propensity for leakage. Moreover, the advancement of CRNV entails the recruitment of inflammatory cells, thereby intensifying corneal edema and inflammation, which may ultimately culminate in fibrosis. In comparison to PBS and CP NPs, the other groups (Dexp, INS, and CPI NPs) exhibited a relatively reduced presence of inflammatory cells, mild edema in the corneal stroma, and neovascular lumen could be observed. On day 14, the corneal tissue in both the PBS and CP NPs groups remained relatively loose and edema-

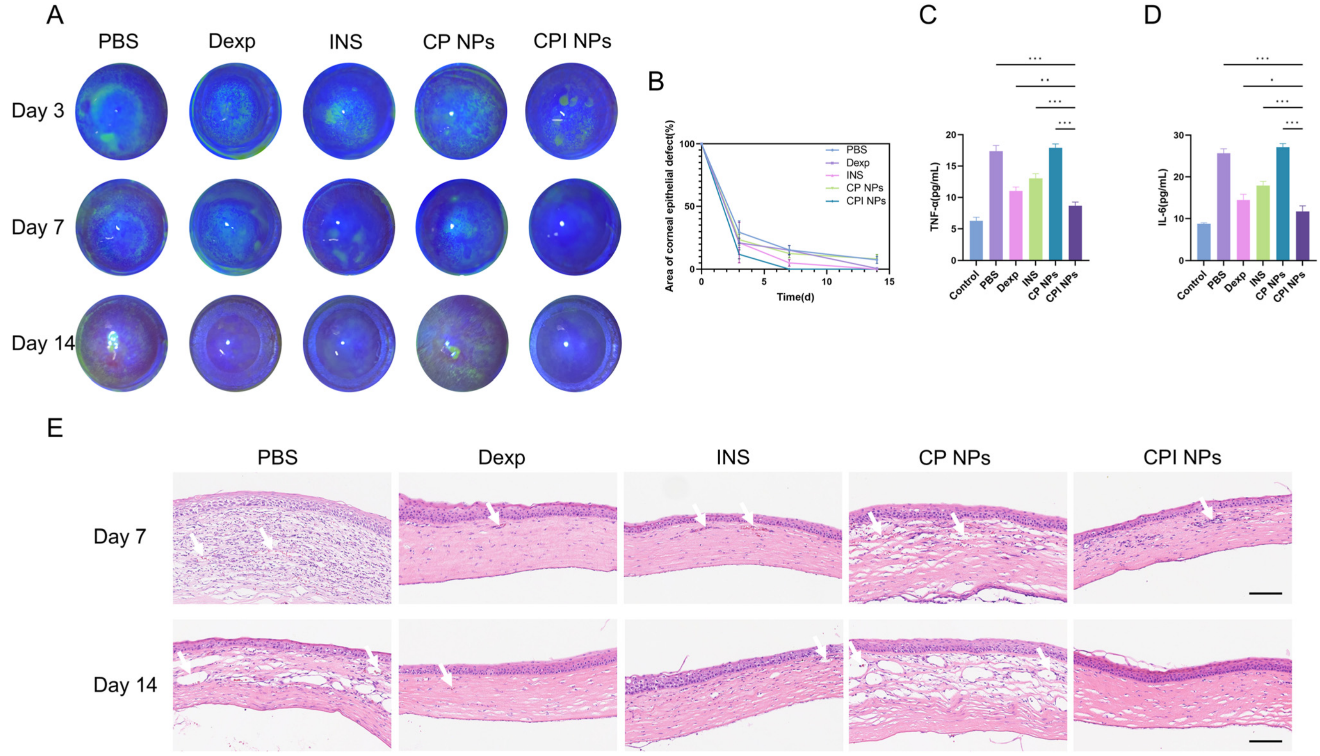

Fig. 5 Changes in the corneal epithelial injury area over time in different groups and *in vivo* suppression of inflammation and neovascularization by CPI NPs. (A) Slit lamp images after fluorescein sodium staining in each group at different time points (days 3, 7, and 14). (B) The percentage of corneal epithelial defect area over time ($n = 3$ per group). (C) TNF- α and IL-6 (D) in cornea of each group after treatment ($n = 3$ per group). (E) HE stained images of rat corneal tissue sections on day 7 and day 14 after alkali burns in each group. The white arrows indicate the sites of neovascularization formation. Scale bar: 100 μm. Results were presented as mean ± SD. $^*p < 0.05$; $^{**}p < 0.01$; $^{***}p < 0.001$.

tous, with a substantial presence of prominent neovascular lumens observed within the stromal layer. Additionally, the infiltration of inflammatory cells in the PBS group was reduced compared to previous observations. In the Dexp group, a few neovascular lumens were observed, with no significant infiltration of inflammatory cells. In the INS group, the stromal layer exhibited a slightly loose arrangement, accompanied by the presence of some neovascularization lumens and minor inflammatory cell infiltration. In contrast, the corneal structure in the CPI NPs group remained intact, with no evident inflammatory cell infiltration and no significant neovascular lumens observed (Fig. 5E).

The progression of CRNV is governed by a multifaceted interplay of factors, primarily stemming from an imbalance between pro-angiogenic and anti-angiogenic factors. The cytokine VEGF is one of the key factors in CRNV, and it is also a target of clinical treatment.[53] VEGF is acknowledged for its ability to stimulate endothelial cell mitosis and promote the joining of adjacent blood vessels into the vascular plexus, resulting in neovascularization.[54] On day 7, the PBS group and CP NPs group presented abundant red fluorescence in the corneal stromal layer, indicating high expression of VEGF. The expression of VEGF in the corneal endothelial layer was higher in the CP NPs group compared to the PBS group. In both the Dexp and INS groups, red fluorescence predominantly localized within the corneal stroma, with minimal red fluorescence observed in the endothelial layer. In the CPI NPs group, red fluorescence was predominantly observed in the stroma and the endothelial layer of the cornea, with a weaker intensity compared to the PBS group. On day 14, the red fluorescence of the corneal layers in the PBS, Dexp, INS, and CP NPs groups exhibited a significant enhancement compared to day 7. In contrast, the increase in red fluorescence intensity observed in the CPI NPs group was the least pronounced among all groups, suggesting that the inhibition of VEGF expression was more effective in the CPI NPs group (Fig. 6A).

CD31, located at the tight junctions between endothelial cells, is integral to the process of angiogenesis and serves as a marker for vascular endothelial cells. And its high expression suggests active proliferation of endothelial cells.[55] Therefore, we assessed the efficacy of each treatment in inhibiting CRNV by detecting the expression of CD31. On day 7, A substantial amount of red fluorescence was detected in the PBS group, with numerous red lumens identified within the corneal stroma layer. The CP NPs group exhibited reduced red fluorescence compared to the PBS group, and multiple red lumens were additionally observed within the stromal layer. A minimal level of red fluorescence was detected in the Dexp group, INS group, and CPI NPs group. On day 14, the formed lumen of the corneal stroma was more pronounced in both the PBS and

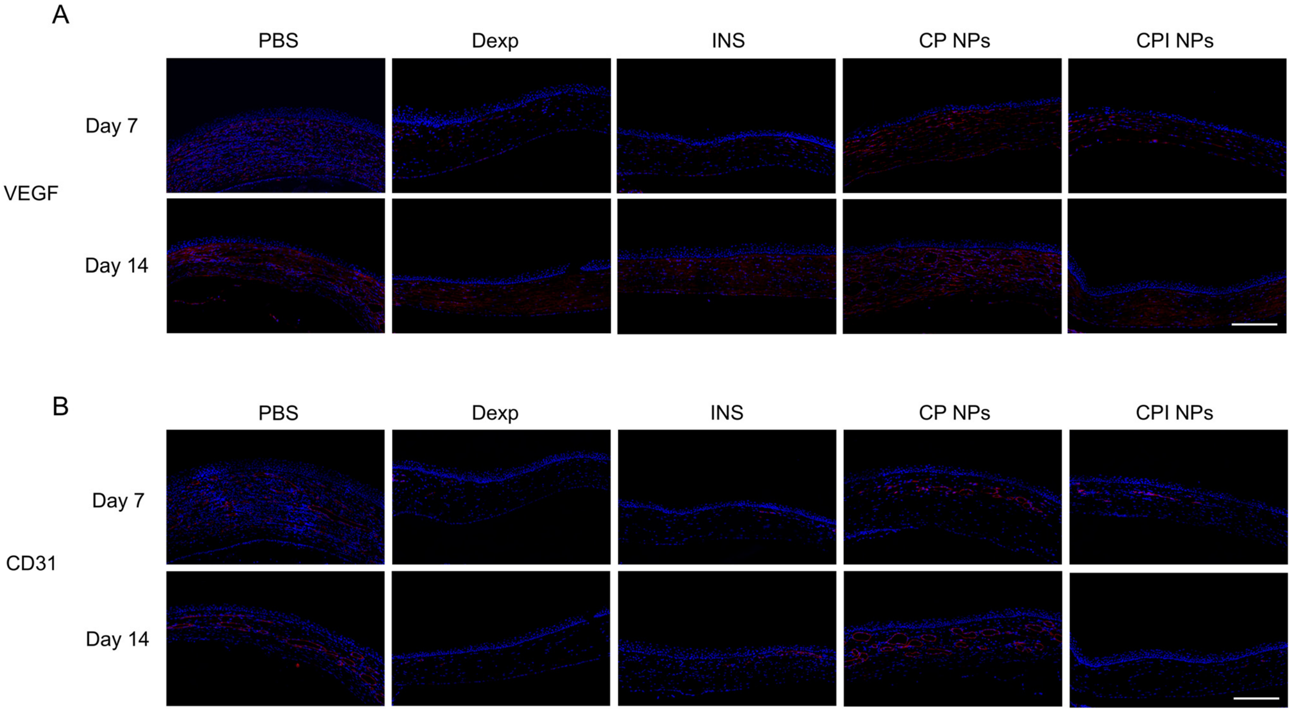

Fig. 6 Immunofluorescence. (A) Immunofluorescence staining of VEGF expression in the corneal tissue after treatment with various formulations at different time points (days 7 and 14). VEGF (red); DAPI (blue). Scale bar: 200 μm. (B) Immunofluorescence staining of CD31 expression in the corneal tissue after treatment with various formulations at different time points (days 7 and 14). CD31 (red); DAPI (blue). Scale bar: 200 μm.

CP NPs groups compared to day 7. In the INS group, two lumens were faintly discernible, whereas in the Dexp and CPI NPs groups, no red lumen was detected, only very weak red fluorescence was observed (Fig. 6B). These findings were largely in agreement with the results obtained from HE staining, suggesting that CPI NPs exert a substantial inhibitory effect on neovascularization.

3.5. Quantitative proteomics

On the 14th day following alkali burn, corneal tissues from the PBS group and INS group were harvested for proteomic sequencing ($n = 3$). The main results of the quantitative proteomics were shown in Fig. 7A–D. Based on the proteomics data, we identified 141 differentially expressed proteins (DEPs) (p-value <0.05 and fold change ≥1.2), of which 63 proteins were upregulated, and 78 proteins were downregulated (Fig. 7A and B). On the basis of these DEPs, GO analysis and KEGG analysis were performed. In the GO secondary classification, biological process mainly included regulation of biological process, cellular metabolic process and organic substance metabolic process. The cellular component classification revealed that most DEPs were located in intracellular anatomical structure, organelle, and cytoplasm. And the molecular function mainly consists of protein binding, ion binding, and organic cyclic compound binding (Fig. 7C). KEGG pathway analysis revealed the pathways significantly enriched in relation to the DEPs. The top five pathways were the cGMP-PKG signaling pathway, aldosterone synthesis and secretion, pancreatic secretion, dopaminergic synapse, and mineral absorption (Fig. 7D). It is worth noting that the cGMP-PKG signaling pathway plays an important role in regulating cell proliferation and apoptosis.[56] Studies have shown that activation of this pathway promotes endothelial cell growth and migration by upregulating VEGF, thereby driving angiogenesis in ischemic diseases.[57,58] In addition, activation of this pathway has been found to promote angiogenesis in breast cancer by regulating the expression of PYCR1,[59] and to promote angiogenesis in nasopharyngeal carcinoma through the regulation of MYLK expression.[60] Therefore, we speculate that the cGMP-PKG signaling pathway plays an important role in INS treatment of CRNV therapy, and its specific regulatory mechanisms still require further research.

3.6. CPI NPs may treat CRNV by influencing m6A modification

On the basis of a review of the relevant literature and combined with the proteomics results, we primarily focused on obesity-associated protein FTO among the differentially expressed proteins. Based on DIA quantitative proteomics, we found that the expression of the m6A demethylase FTO was significantly downregulated in INS-treated neovascularized corneas. The main function of FTO is to reduce m6A levels through its demethylase activity. m6A is the most common internal chemical modification of mRNA in eukaryotes and is involved in various biological processes. It plays an important role in the regulation of RNA fate and function, including mRNA splicing, transport, stability, translation, primary

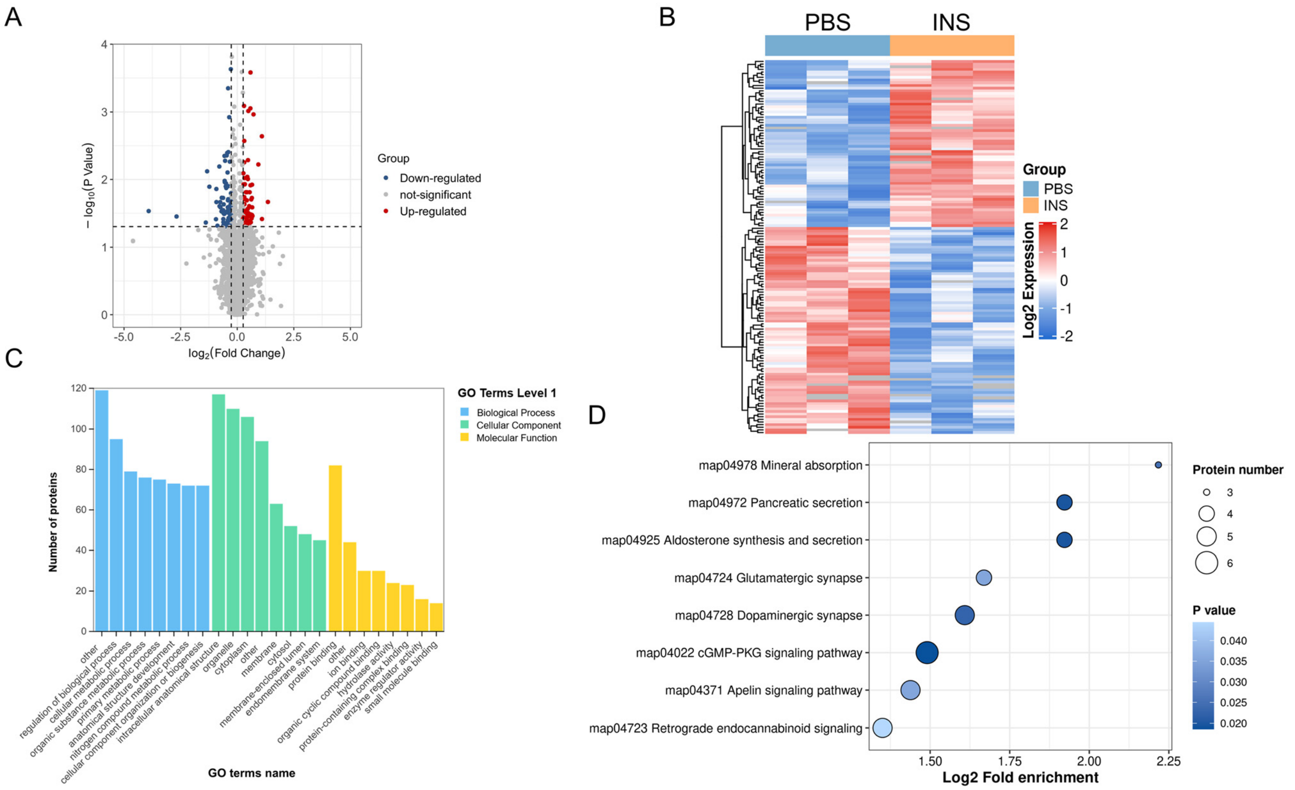

Fig. 7 Quantitative proteomics. (A) Volcano plot of DEPs. Upregulated proteins were represented in red, downregulated ones in blue, and proteins without differential expression in gray. (B) The heat map showed differentially expressed proteins in different samples from different groups, with red representing high expression and blue representing low expression. (C) Classification of GO, bar chart represents the top 8 GO terms. (D) We performed KEGG pathway enrichment analysis for differentially expressed proteins in each comparison group.

microRNA maturation, and RNA–protein interactions. m6A modification is a dynamic and reversible process, that is catalyzed by the METTL3-METTL14-WTAP methyltransferase complex and removed by demethylases such as FTO and ALKBH5.[61] FTO is the first RNA demethylase discovered in the cell nucleus, it plays a key role in regulating m6A modification, and has been found to be involved in the progression of various diseases.[62] FTO-catalyzed m6A demethylation regulates the expression of lipid-related genes and is involved in lipid metabolism and lipid dysregulation diseases.[63] Targeting FTO offers promising therapeutic potential by inhibiting tumor growth, enhancing the effectiveness of immunotherapy, and reducing drug resistance.[64] A clinical study revealed that variations in the FTO gene might have contributed to the development of cardiovascular diseases in men with glucose metabolism abnormalities.[65] In addition, a study by Mathiyalagan *et al.* was conducted on mouse myocardial infarction confirmed that overexpression of FTO could reduce myocardial fibrosis in ischemic hearts and promote angiogenesis.[66] They also reported that FTO acts on multiple pathways associated with angiogenesis. A study by Rong *et al.* investigated the role of m6A modification in angiogenesis in intrahepatic cholangiocarcinoma.[67] These results indicate that reduced expression of FTO affects tumor angiogenesis in intrahepatic cholangiocarcinoma. A recent study confirmed that FTO overexpression triggered a series of diabetic retinal pathological phenotypes, including angiogenesis, vascular leakage, inflammation, and neurodegeneration. These changes are mediated by directly affecting endothelial cell characteristics and regulating the interactions between endothelial cells and pericytes/microglia.[68] However, the regulatory role of m6A modification in CRNV induced by alkali burns under INS treatment has not been studied or reported.

To investigate the effects of m6A modification on CRNV after CPI NPs treatment, we first analyzed corneal FTO protein levels before and after treatment with CPI NPs treatment. The results revealed that, in the neovascularization corneas, the protein expression of FTO was significantly increased, whereas CPI NPs treatment reduced the FTO protein level (Fig. 8A and B). Next, we quantified the m6A modification in the cornea of the control group, the CRNV group, and the CPI NPs treated group, as shown in Fig. 8C. CPI NPs treatment resulted in a significant increase in m6A modification compared to the levels observed in the CRNV group. After CPI NPs treatment, FTO mRNA expression was reduced in the neovascularized corneas (Fig. 8D). We treated HUVECs with LPS to simulate the pathological conditions of endothelial cells during CRNV. Compared to the control group cells, the expression of FTO at both the mRNA and protein levels was significantly upregulated in LPS-induced HUVECs, and m6A modification

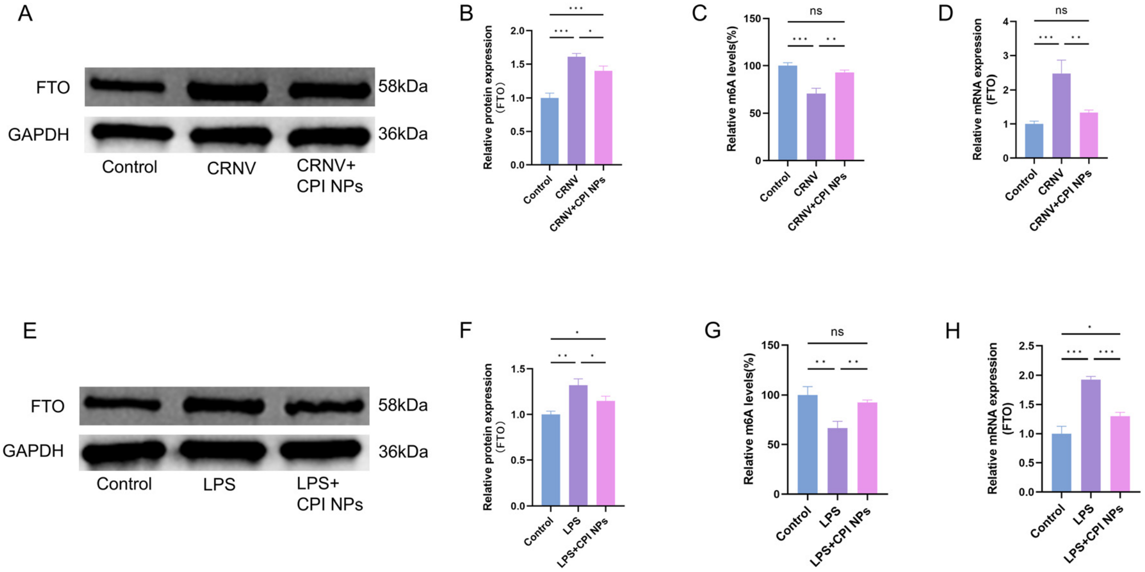

Fig. 8 The CPI NPs may treat CRNV by upregulating m6A modification. (A and B) The protein expression of FTO in cornea (n = 3). (C) Quantification of m6A in total corneal RNA was determined by colorimetric method (n = 3). (D) qRT-PCR showing mRNA expression of FTO in cornea (n = 3). (E and F) The protein expression of FTO in HUVECs (n = 3). (G) Quantification of m6A in total HUVECs RNA was determined by colorimetric method (n = 3). (H) qRT-PCR showing mRNA expression of FTO in HUVECs (n = 3). Results were presented as mean ± SD. ns indicates no significant difference. $^{*}p < 0.05$; $^{**}p < 0.01$; $^{***}p < 0.001$.

was significantly decreased. In contrast, CPI NPs treatment counteracted the upregulation of FTO expression and the decrease of m6A modification in LPS-induced HUVECs (Fig. 8E–H).

In conclusion, the decrease of FTO-mediated m6A modification may play an important role in alkali burn-induced CRNV, and the treatment of alkali burn-induced CRNV with CPI NPs may inhibit FTO expression, promote m6A modification, and thereby suppress the formation of CRNV.

3.7. Biocompatibility

The biocompatibility of CPI NPs is crucial for their effective translation into clinical applications.[69] The biocompatibility of various eye drop formulations was assessed in normal rats over 14 days. The results showed no corneal opacity, defects, neovascularization, inflammation, or congestion. In addition, the integrity of the corneal epithelium was assessed by sodium fluorescein staining, and no significant fluorescent staining was detected. The above results indicated that CPI NPs has no obvious toxic and side effects on the anterior segment of the eye during treatment, and was relatively safe. In addition, HE staining revealed that the whole layer of the cornea was arranged completely, and no inflammatory cells or angiogenesis was found (Fig. 9A and B).

Following a 14-day regimen of various eye drop formulations, HE staining of major organs, including the liver, heart, lung, kidney, and spleen, indicated no significant pathological abnormalities (Fig. 9C). Furthermore, the findings from serum biochemistry and complete blood count analyses in rats demonstrated that hepatic and renal function indicators, including aspartate aminotransferase (AST), blood urea nitrogen (BUN), and creatinine (CREA) levels, did not exhibit significant differences. Additionally, the complete blood cell counts for each group, encompassing white blood cell (WBC), red blood cell (RBC), and platelet (PLT) counts, remained within normal physiological ranges (Fig. 9D).

These findings suggested that the CPI NPs were a novel eye drop formulation with minimal ocular irritation and systemic toxicity, indicating a strong safety profile and promising clinical potential.

3.8. Degradation evaluation

The residual weight of CPI NPs samples exhibited a significant downward trend on the first day, the residual weight decreased to about 92.3%. Subsequently, the samples showed a continuous degradation trend, and the residual weight decreased to about 76.1% on day 7. On day 21, the residual weight of samples dropped to about 62.8% (ESI Fig. 2†). The findings indicated that the CPI NPs gradually released drugs through hydrolysis *in vitro*. This degradation behavior aligns with the degradation kinetics observed in most polyester materials, which is conducive to maintaining a stable drug release rate and avoiding sudden release effect.

After intravenous injection *via* the tail vein, the relative fluorescence intensity of the blood collected at a certain interval was measured by a fluorescence microplate reader to evaluate the circulation of the nanomedicine *in vivo*. The results showed that the residual fluorescence of DiI-CPI NPs in the blood was approximately 39.1% at 24 h, about 4.1% at 72 h, and almost no DiI-CPI NPs remained in the blood at 96 h (0.4%) (ESI Fig. 3†). These results suggested that the DiI-CPI

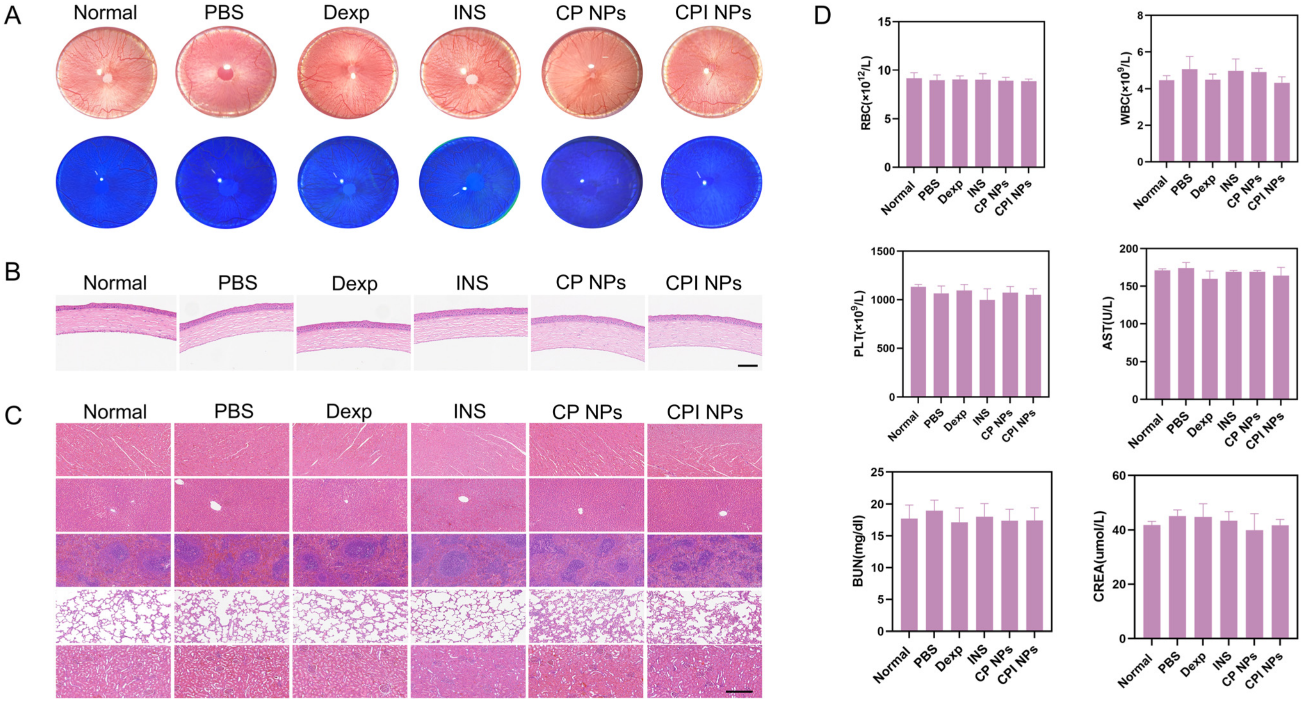

Fig. 9 Biocompatibility of the CPI NPs *in vivo*. On day 14, the *in vivo* biocompatibility of the groups treated with different formulations, as well as the normal group (no administration), was assessed using slit lamp examination, fluorescein sodium staining (A), and HE staining (B) after 14 days of administering various reagents three times daily. Scale bar: 100 μm; *n* = 3. (C) HE staining of the heart, liver, spleen, lung and kidney of rats after different treatments. scale bar: 200 μm. (D) Blood biochemical analysis of rats after different treatments; *n* = 3.

NPs were almost entirely degraded and metabolized following 96 h of *in vivo* circulation.

4. Conclusion

In this study, a CPI NPs drug delivery system was developed by incorporating INS into CS and PLGA, which exhibited anti-inflammatory, anti-angiogenic, and m6A-modulating properties, along with good biosafety. In a rat model of CRNV, CPI NPs significantly alleviated alkali burn-induced CRNV. The anti-angiogenic effects of CPI NPs were validated through endothelial cell migration and tube formation assays. To the best of our knowledge, this is the first study to use a CS-PLGA nanosystem to deliver INS as a treatment for CRNV. In addition, through proteomic analysis, we identified DEPs and found that the therapeutic mechanism of CPI NPs may be related to the regulation of m6A modification. Preliminary evidence suggested a reduction in m6A modification levels in alkali burn-induced CRNV. Furthermore, both *in vitro* and *in vivo* studies have verified that CPI NPs treatment enhanced m6A modification. This is also the first report to demonstrate that INS affects m6A modification. This study may provide a new potential target for drug therapy for CRNV. The CPI nanoparticle delivery system showed potential as an effective, straightforward, and safe alternative for the treatment of alkali burn-induced CRNV, potentially providing novel therapeutic options for a substantial population of CRNV patients. In future research, we intend to further validate the efficacy and safety of CPI NPs through additional animal studies, with the objective of confirming their potential for clinical application and investigating their role in other ophthalmic diseases.

Author contributions

Yuqing Zhang: writing – review & editing, writing – original draft, validation, methodology, investigation, formal analysis, data curation. Yangrui Du: writing – original draft, conceptualization, methodology, validation, investigation, data curation. Sijie Zhou: methodology, writing – review & editing, visualization. Zeqi Liu: investigation, data curation. Pan Li: validation, supervision. Zhiyu Du: writing – review & editing, supervision, project administration, funding acquisition.

Data availability

The data supporting this article have been included as part of the ESI.†

Conflicts of interest

There are no conflicts of interest to declare.

Acknowledgements

This study was supported by the grant from the Key Program of Chongqing Natural Science Foundation (No. cstc2021ycjh-bgzxm0064).

References

1 W. Cho, S. K. Mittal, E. Elbasiony and S. K. Chauhan, *Ocul. Surf.*, 2020, **18**, 857–864.
2 W. Huang, L. Wang, R. Yang, R. Hu, Q. Zheng and X. Zan, *Mater. Today Bio*, 2022, **17**, 100456.
3 D. Roshandel, M. Eslani, A. Baradaran-Rafii, A. Y. Cheung, K. Kurji, S. Jabbehdari, A. Maiz, S. Jalali, A. R. Djalilian and E. J. Holland, *Ocul. Surf.*, 2018, **16**, 398–414.
4 K. Wang, L. Jiang, Y. Zhong, Y. Zhang, Q. Yin, S. Li, X. Zhang, H. Han and K. Yao, *Bioeng. Transl. Med.*, 2021, **7**, e10276.
5 A. Bakunowicz-Łazarczyk and B. Urban, *Adv. Med. Sci.*, 2016, **61**, 101–112.
6 P. Rama, S. Matuska, G. Paganoni, A. Spinelli, M. De Luca and G. Pellegrini, *N. Engl. J. Med.*, 2010, **363**, 147–155.
7 M. Soleimani and M. Naderan, *Clin. Ophthalmol.*, 2020, **14**, 2687–2699.
8 H. Zhang, K. Zhang, Q. S. Zhang, L. Wang, Y. H. Gao, G. Y. Xu, D. Long, H. Wang and Y. Hu, *J. Controlled Release*, 2023, **362**, 715–725.
9 W. Stevenson, S. F. Cheng, M. H. Dastjerdi, G. Ferrari and R. Dana, *Ocul. Surf.*, 2012, **10**, 67–83.
10 S. Yang, Y. Zhang, Z. Zhang, J. Dan, Q. Zhou, X. Wang, W. Li, L. Zhou, L. Yang and L. Xie, *Am. J. Pathol.*, 2020, **190**, 2237–2250.
11 E. M. Rocha, M. H. de M Lima, C. R. Carvalho, M. J. Saad and L. A. Velloso, *Curr. Eye Res.*, 2000, **21**, 833–842.
12 S. T. Feldman, D. Gately, B. L. Seely, A. Schonthal and J. R. Feramisco, *Invest. Ophthalmol. Visual Sci.*, 1993, **34**, 2105–2111.
13 T. R. Aynsley, *Br. J. Ophthalmol.*, 1945, **29**, 361–363.
14 M. Jaworski, A. Lorenc, R. Leszczyński and E. Mrukwa-Kominek, *Pharmaceutics*, 2023, **16**, 15.
15 S. Balal, N. Din, C. Ashton and S. Ahmad, *Cornea*, 2023, **42**, 1000–1004.
16 D. Diaz-Valle, B. Burgos-Blasco, D. Rego-Lorca, V. Puebla-Garcia, P. Perez-Garcia, J. M. Benitez-Del-Castillo, R. Herrero-Vanrell, M. Vicario-de-la-Torre and J. A. Gegundez-Fernandez, *Acta Ophthalmol.*, 2022, **100**, e912–e919.
17 Y. Song, W. Ding, Y. Bei, Y. Xiao, H. D. Tong, L. B. Wang and L. Y. Ai, *Biomed. Pharmacother.*, 2018, **104**, 474–484.
18 A. M. Dasrilsyah, W. H. Wan Abdul Halim, M. Mustapha, S. F. Tang, B. Kaur, E. Y. Ong and M. L. C. Bastion, *Cornea*, 2023, **42**, 1395–1403.
19 D. R. Janagam, L. Wu and T. L. Lowe, *Adv. Drug Delivery Rev.*, 2017, **122**, 31–64.
20 H. Han, S. Li, M. Xu, Y. Zhong, W. Fan, J. Xu, T. Zhou, J. Ji, J. Ye and K. Yao, *Adv. Drug Delivery Rev.*, 2023, **196**, 114770.
21 Y. Wang, L. Zhou, L. Fang and F. Cao, *Acta Biomater.*, 2020, **104**, 104–114.
22 J. F. Fangueiro, F. Veiga, A. M. Silva and E. B. Souto, *Curr. Pharm. Des.*, 2016, **22**, 1135–1146.
23 F. Danhier, E. Ansorena, J. M. Silva, R. Coco, A. Le Breton and V. Préat, *J. Controlled Release*, 2012, **161**, 505–522.
24 S. K. Shahbaz, K. Koushki, T. Sathyapalan, M. Majeed and A. Sahebkar, *Curr. Neuropharmacol.*, 2022, **20**, 309–323.
25 D. Xu, X. J. Song, X. Chen, J. W. Wang and Y. L. Cui, *J. Controlled Release*, 2024, **367**, 366–384.
26 J. Zhu, F. Qin, Z. Ji, W. Fei, Z. Tan, Y. Hu and C. Zheng, *AAPS PharmSciTech*, 2019, **21**, 13.
27 J. Yang, H. Zeng, Y. Luo, Y. Chen, M. Wang, C. Wu and P. Hu, *Polymers*, 2024, **16**, 2606.
28 M. J. Ramalho, E. Serra, J. Lima, J. A. Loureiro and M. C. Pereira, *Eur. J. Pharm. Biopharm.*, 2024, **200**, 114326.
29 Z. Qin, B. Li, Q. Deng, Y. Wen, S. Feng, C. Duan, B. Zhao, H. Li, Y. Gao and J. Ban, *Molecules*, 2024, **29**, 658.
30 L. Bai, Q. Han, Z. Han, X. Zhang, J. Zhao, H. Ruan, J. Wang, F. Lin, W. Cui, X. Yang and Y. Hao, *Adv. Healthcare Mater.*, 2024, **13**, e2302327.
31 M. A. Matica, F. L. Aachmann, A. Tøndervik, H. Sletta and V. Ostafe, *Int. J. Mol. Sci.*, 2019, **20**, 5889.
32 H. Zali, M. Zamanian-Azodi, M. Rezaei Tavirani and A. Akbar-Zadeh Baghban, *Iran. J. Pharm. Res.*, 2015, **14**, 291–302.
33 C. Anderson, Q. Zhou and S. Wang, *J. Visualized Exp.*, 2014, 51159.
34 P. S. Bhattacharjee, T. S. Huq, T. K. Mandal and R. A. Graves, *PLoS One*, 2011, **6**, e15905.
35 M. Li, X. Yu, L. Zhu, Y. Jin and Z. Wu, *Drug Delivery*, 2021, **28**, 206–217.
36 R. Suri, Y. R. Neupane, N. Mehra, M. Nematullah, F. Khan, O. Alam, A. Iqubal, G. K. Jain and K. Kohli, *Int. J. Biol. Macromol.*, 2021, **191**, 548–559.
37 A. C. Amrite, H. F. Edelhauser, S. R. Singh and U. B. Kompella, *Mol. Vision*, 2008, **14**, 150–160.
38 H. Yao, H. Xu, M. Wu, W. Lei, L. Li, D. Liu, Z. Wang, H. Ran, H. Ma and X. Zhou, *Acta Biomater.*, 2023, **166**, 536–551.
39 S. Taghavi, M. Ramezani, M. Alibolandi, K. Abnous and S. M. Taghdisi, *Cancer Lett.*, 2017, **400**, 1–8.
40 M. Sousa de Almeida, E. Susnik, B. Drasler, P. Taladriz-Blanco, A. Petri-Fink and B. Rothen-Rutishauser, *Chem. Soc. Rev.*, 2021, **50**, 5397–5434.
41 A. Meza-Rios, J. Navarro-Partida, J. Armendariz-Borunda and A. Santos, *Ophthalmol. Ther.*, 2020, **9**, 1–14.
42 G. Coco, G. Buffon, A. Taloni and G. Giannaccare, *Nanomaterials*, 2024, **14**, 669.
43 M. Bin-Jumah, S. J. Gilani, M. A. Jahangir, A. Zafar, S. Alshehri, M. Yasir, C. Kala, M. Taleuzzaman and S. S. Imam, *Int. J. Nanomed.*, 2020, **15**, 7861–7875.

44 S. Wang, X. Li, M. Parra, E. Verdin, R. Bassel-Duby and E. N. Olson, *Proc. Natl. Acad. Sci. U. S. A.*, 2008, **105**, 7738–7743.

45 V. Mariotti, R. Fiorotto, M. Cadamuro, L. Fabris and M. Strazzabosco, *Jhep Rep.*, 2021, **3**, 100251.

46 L. Wang and H. K. W. Law, *Int. J. Mol. Sci.*, 2019, **20**, 5281.

47 Q. Luo, J. Yang, H. Xu, J. Shi, Z. Liang, R. Zhang, P. Lu, G. Pu, N. Zhao and J. Zhang, *Drug Delivery*, 2022, **29**, 837–855.

48 X. Xiong, H. Jiang, Y. Liao, Y. Du, Y. Zhang, Z. Wang, M. Zheng and Z. Du, *Bioeng. Transl. Med.*, 2023, **8**, e10499.

49 H. Shimizu, T. Sakimoto and S. Yamagami, *Sci. Rep.*, 2019, **9**, 9596.

50 S. Li, K. Pang, S. Zhu, K. Pate and J. Yin, *Nat. Commun.*, 2022, **13**, 7371.

51 C. H. Dohlman, C. Zhou, F. Lei, F. Cade, C. V. Regatieri, A. Črnej, J. G. Dohlman, L. Q. Shen and E. I. Paschalis, *Cornea*, 2019, **38**, 1589–1594.

52 A. M. Ibrahim Al-Mashahedah, R. K. Kanwar and J. R. Kanwar, *Nanomedicine*, 2019, **14**, 1049–1072.

53 N. Nieto-Nicolau, E. M. Martínez-Conesa, S. Fuentes-Julián, F. Arnalich-Montiel, I. García-Tuñón, M. P. De Miguel and R. P. Casaroli-Marano, *J. Cell. Mol. Med.*, 2021, **25**, 5124–5137.

54 X. Li, Y. Gao, J. Li, K. Zhang, J. Han, W. Li, Q. Hao, W. Zhang, S. Wang, C. Zeng, W. Zhang, Y. Zhang, M. Li and C. Zhang, *Cell Death Dis.*, 2018, **9**, 744.

55 W. Ma, X. Zhang, Y. Liu, L. Fan, J. Gan, W. Liu, Y. Zhao and L. Sun, *Adv. Sci.*, 2022, **9**, e2103317.

56 S. Ali, A. S. Solano, A. L. Gonzales, P. Thakore, V. Krishnan, E. Yamasaki and S. Earley, *Function*, 2021, **2**, zqab051.

57 M. A. Bayarri, J. Milara, C. Estornut and J. Cortijo, *Front. Physiol.*, 2021, **12**, 687381.

58 S. Chen, L. Lv, Z. Zhan, X. Wang, Z. You, X. Luo and H. You, *J. Cell. Physiol.*, 2020, **235**, 7757–7768.

59 B. Cui, B. He, Y. Huang, C. Wang, H. Luo, J. Lu, K. Su, X. Zhang, Y. Luo, Z. Zhao, Y. Yang, Y. Zhang, F. An, H. Wang, E. W. Lam, K. W. Kelley, L. Wang, Q. Liu and F. Peng, *Cell Death Dis.*, 2023, **14**, 682.

60 H. Wang, W. Wang and S. Fan, *Int. J. Biol. Sci.*, 2022, **18**, 2714–2728.

61 H. Shi, J. Wei and C. He, *Mol. Cell*, 2019, **74**, 640–650.

62 G. Jia, Y. Fu, X. Zhao, Q. Dai, G. Zheng, Y. Yang, C. Yi, T. Lindahl, T. Pan, Y. G. Yang and C. He, *Nat. Chem. Biol.*, 2011, **7**, 885–887.

63 Z. Yang, G. L. Yu, X. Zhu, T. H. Peng and Y. C. Lv, *Genes Dis.*, 2021, **9**, 51–61.

64 Y. Li, R. Su, X. Deng, Y. Chen and J. Chen, *Trends Cancer*, 2022, **8**, 598–614.

65 T. Lappalainen, M. Kolehmainen, U. S. Schwab, A. M. Tolppanen, A. Stančáková, J. Lindström, J. G. Eriksson, S. Keinänen-Kiukaanniemi, S. Aunola, P. Ilanne-Parikka, C. Herder, W. Koenig, H. Gylling, H. Kolb, J. Tuomilehto, J. Kuusisto, M. Uusitupa and Finnish Diabetes Prevention Study Group, *Nutr., Metab. Cardiovasc. Dis.*, 2011, **21**, 691–698.

66 P. Mathiyalagan, M. Adamiak, J. Mayourian, Y. Sassi, Y. Liang, N. Agarwal, D. Jha, S. Zhang, E. Kohlbrenner, E. Chepurko, J. Chen, M. G. Trivieri, R. Singh, R. Bouchareb, K. Fish, K. Ishikawa, D. Lebeche, R. J. Hajjar and S. Sahoo, *Circulation*, 2019, **139**, 518–532.

67 Z. X. Rong, Z. Li, J. J. He, L. Y. Liu, X. X. Ren, J. Gao, Y. Mu, Y. D. Guan, Y. M. Duan, X. P. Zhang, D. X. Zhang, N. Li, Y. Z. Deng and L. Q. Sun, *Front. Oncol.*, 2019, **9**, 369.

68 X. Chen, Y. Wang, J. N. Wang, Y. C. Zhang, Y. R. Zhang, R. X. Sun, B. Qin, Y. X. Dai, H. J. Zhu, J. X. Zhao, W. W. Zhang, J. D. Ji, S. T. Yuan, Q. D. Shen and Q. H. Liu, *EMBO Mol. Med.*, 2024, **16**, 294–318.

69 A. M. Bossi, A. Bucciarelli and D. Maniglio, *ACS Appl. Mater. Interfaces*, 2021, **13**, 31431–31439.